Supplemental Material: Determining Dark Matter-Electron Scattering Rates from the Dielectric Function

Yonit Hochberg,[1] Yonatan Kahn,[2,3] Noah Kurinsky,[4,5] Benjamin V. Lehmann,[6,7] To Chin Yu,[8,9] and Karl K. Berggren[10]

[1] *Racah Institute of Physics, Hebrew University of Jerusalem, Jerusalem 91904, Israel*
[2] *Department of Physics, University of Illinois at Urbana-Champaign, Urbana, IL 61801, USA*
[3] *Illinois Center for Advanced Studies of the Universe, University of Illinois at Urbana-Champaign, Urbana, IL 61801, USA*
[4] *Fermi National Accelerator Laboratory, Batavia, IL 60510, USA*
[5] *Kavli Institute for Cosmological Physics, University of Chicago, Chicago, Illinois 60637, USA*
[6] *Department of Physics, University of California Santa Cruz, Santa Cruz, CA 95064, USA*
[7] *Santa Cruz Institute for Particle Physics, Santa Cruz, CA 95064, USA*
[8] *Department of Physics, Stanford University, Stanford, CA 94305, USA*
[9] *SLAC National Accelerator Laboratory, 2575 Sand Hill Road, Menlo Park, CA 94025, USA*
[10] *Massachusetts Institute of Technology, Department of Electrical Engineering and Computer Science, Cambridge, MA 02139, USA*

Updated December 20, 2022: a typographical error has been corrected in Eq. (S.16), and we have clarified that $\lambda_{\rm TF}$ is the inverse of the Thomas–Fermi screening length. Our conclusions are unchanged.

In this Supplemental Material, we provide a number of derivations and further details to support the results in the main Letter. Section I derives our main result for the DM scattering rate in terms of the loss function. Section II outlines a number of simple analytic models for dielectric functions in various materials, and compares them to measured data for Al (representative of an ordinary superconductor), Si (a typical semiconductor), and URu_2Si_2 (an example of a heavy-fermion superconductor with meV-scale plasmons). We compare the free-electron gas (FEG) model for Si to the spectrum computed using crystal form factors generated by the publicly-available `QEdark` code [3], and show good qualitative agreement in the range 5–15 eV. Section III is devoted to a detailed comparison of our results for superconductors with other results in the literature, justifying our claim of a stronger reach by several orders of magnitude compared to previous estimates, and gives the projected reach for heavy mediators.

I. SCATTERING RATE IN TERMS OF THE LOSS FUNCTION

Here we derive Eq. (1) and show how the scattering rate for all spin-independent DM-electron interactions is governed by the loss function. Suppose DM couples to electrons through a low-energy Hamiltonian of the form

$$\hat{H}_{\rm int} = \sum_i V(\hat{\mathbf{r}}_\chi - \hat{\mathbf{r}}_i), \tag{S.1}$$

where the sum runs over all electrons in the target. Fourier transforming the potential,

$$V(\hat{\mathbf{r}}_\chi - \hat{\mathbf{r}}_i) = \int \frac{\mathrm{d}^3\mathbf{q}}{(2\pi)^3} e^{i\mathbf{q}\cdot(\hat{\mathbf{r}}_\chi - \hat{\mathbf{r}}_i)} V(\mathbf{q}), \tag{S.2}$$

we can write the interaction Hamiltonian as

$$\hat{H}_{\rm int} = \int \frac{\mathrm{d}^3\mathbf{q}}{(2\pi)^3} e^{i\mathbf{q}\cdot\hat{\mathbf{r}}_\chi} V(\mathbf{q})\hat{\rho}(\mathbf{q}), \tag{S.3}$$

where the momentum-space electron density operator is defined as

$$\hat{\rho}(\mathbf{q}) = \int \mathrm{d}^3\mathbf{x} \sum_i \delta(\mathbf{x} - \hat{\mathbf{r}}_i) e^{-i\mathbf{q}\cdot\mathbf{x}} = \sum_i e^{-i\mathbf{q}\cdot\hat{\mathbf{r}}_i}. \tag{S.4}$$

By Fermi's Golden Rule (equivalently, the Born approximation), we can compute the transition rate $\Gamma(\mathbf{v}_\chi)$ from the ground state $|0\rangle$ for a given incoming DM velocity $\mathbf{v}_\chi$, treating the incoming and outgoing DM as plane waves with energy and momentum $(E_\chi, \mathbf{p}_\chi)$ and $(E'_\chi, \mathbf{p}'_\chi)$ respectively. We take the ground state to have zero energy without

loss of generality. The transition rate is given by [25]

$$\begin{aligned}\Gamma(\mathbf{v}_\chi) &= \sum_f \left|\langle f;\mathbf{p}'_\chi|\hat{H}_{\rm int}|0;\mathbf{p}_\chi\rangle\right|^2 2\pi\delta(\omega_f + E'_\chi - E_\chi)\\ &= \int \frac{\mathrm{d}^3\mathbf{q}}{(2\pi)^3}|V(\mathbf{q})|^2 \sum_f \left|\langle f|\hat{\rho}(\mathbf{q})|0\rangle\right|^2 2\pi\delta(\omega_f - \omega_{\mathbf{q}}),\end{aligned} \tag{S.5}$$

where $|f\rangle$ is a final state with energy ω_f and the sum runs over all possible final states of the system, and we recall that

$$\omega_{\mathbf{q}} = \mathbf{q}\cdot\mathbf{v}_\chi - \frac{q^2}{2m_\chi}. \tag{S.6}$$

Note that the only assumption that was made here was that $\hat{H}_{\rm int}$ is sufficiently weak compared to the unperturbed Hamiltonian $\hat{H}_0$ of the target system; this is the case in Ref. [54] for ordinary electron-electron scattering, so it must be the case for DM-electron scattering where the couplings are much weaker. Note this implies one cannot directly apply our result to regions of parameter space where DM and electrons are strongly coupled, as would be relevant for regions in parameter space where DM may not reach underground detectors due to multiple scattering [10–12, 18, 23].

The insight of Ref. [54] is to relate the density matrix element $|\langle f|\hat{\rho}(\mathbf{q})|0\rangle|^2$ to an experimentally measurable quantity, the dielectric function $\epsilon(\mathbf{q},\omega)$. The dielectric function is *defined* as the linear response of the target to the longitudinal electric field of a test charge. For simplicity and to elucidate the formalism, in this work we consider the case of an isotropic material where the dielectric function is a scalar rather than a tensor, and relegate the treatment of the anisotropic case to upcoming work [67]. Since a test charge will also perturb the electron density of the target, it can be shown that this is equivalent to defining the dielectric function as a density-density correlation function [86]. Of course, the electrons will also couple to ions, and strictly speaking the ion density operator should also appear in the measured loss function. In what follows, we will assume that these contributions are negligible, which is the approximation always made in the condensed matter literature. This assumption makes our formalism independent of the DM coupling to protons or neutrons, and even if ion contributions are significant, the measured loss function will give *exactly* the correct rate for a dark photon mediator.

Because the dielectric function is defined as the *linear* response of the system, the same assumptions are implicit in the setup of [54] (with an electromagnetic probe) as are present in the DM scattering setup: the test charge interactions are weak compared to the internal interactions $\hat{H}_0$. Therefore the Coulomb potential of the test charge may be factored out in Fourier space, separating the (weak) perturbation due to the probe and the (possibly strong) response of the system to such a probe. The result is [54, 86]

$$\mathrm{Im}\left(-\frac{1}{\epsilon(\mathbf{q},\omega)}\right) = \frac{\pi e^2}{q^2}\sum_f \left|\langle f|\hat{\rho}(\mathbf{q})|0\rangle\right|^2 \delta(\omega_f - \omega). \tag{S.7}$$

Here we are using Heaviside-Lorenz conventions for the electron charge e as is common in high-energy physics, which differs from the Gaussian unit definition common in condensed matter physics by a factor of $\sqrt{4\pi}$. (Note also that Eq. (9) of [54] is missing a factor of π.) Plugging Eq. (S.7) into Eq. (S.5), we obtain our main result, Eq. (1). For reference, the sum over final states on the right-hand side of Eq. (S.7) is (up to factors of π) conventionally defined in the condensed matter literature as the dynamic structure factor.

Notice that we have made no assumptions whatsoever about the character of the final state $|f\rangle$. It is an exact eigenstate of the (in general very complicated) many-body condensed matter Hamiltonian, and the only requirement is that it represents some rearrangement of the electrons in the target so that it has a nonzero matrix element with the electron density operator with respect to the ground state. In this sense our treatment is distinct from Ref. [25], which defines a general dynamic structure factor (with slightly different normalization compared to the condensed matter conventions) very similar to the sum in Eq. (S.5), but one which is excitation-specific and requires quantization in terms of single-quasiparticle states in the case of electron scattering. When all many-body states are included, the structure factor defined in Ref. [25] for electron scattering is *identical* to the loss function defined through the complex dielectric function, is directly measurable without the need to compute single-particle wavefunctions, and automatically includes all in-medium effects. (Our formalism is philosophically similar to Ref. [87], which parameterizes non-relativistic potentials using only general principles such as the Källén-Lehmann spectral representation, without relying on the assumption of the perturbative exchange of a single mediator.) On the other hand, the formalism of Ref. [25] is useful

when DM couples differently to electrons, protons, and neutrons than the photon, in an energy regime where density perturbations to both electrons and ions are relevant, as might be the case for sub-gap single-phonon excitations.

Finally, we note that other UV Lagrangians considered in Ref. [36] also generate non-relativistic potentials which couple to the electron density, but are often accompanied by other spin- or momentum-dependent operators which may complicate our arguments, so we focus on the case of spin-independent scattering. In particular, if DM is a Dirac fermion χ which couples to a scalar ϕ of mass m_ϕ through the scalar current $\mathcal{L} \supset g_\chi \phi \bar{\chi}\chi$, or to a vector V_μ of mass m_V through the vector current $\mathcal{L} \supset g_\chi V_\mu \bar{\chi}\gamma^\mu \chi$, and if the mediator couples to electrons in an analogous fashion but with coupling g_e, the resulting potential is the same in both cases [36]:

$$V(\mathbf{q}) = V(q) = \frac{g_\chi g_e}{q^2 + m_{\phi,V}^2}. \tag{S.8}$$

Similar formulas apply when DM is a complex scalar. Note that in contrast with Ref. [36], we leave the DM-electron coupling as its 'bare' value and place all in-medium corrections to this coupling entirely within the loss function. In the case where $g_e \propto e$, as would be the case for a kinetically-mixed dark photon mediator or when the DM is millicharged, the factors of $1/e^2$ cancel in Eq. (1) because the DM-induced perturbation to the electron density is exactly proportional to an ordinary electromagnetic probe.

For completeness, we give the expression for the energy spectrum from DM-electron scattering,

$$\frac{\mathrm{d}R}{\mathrm{d}\omega} = \frac{\rho_\chi}{2\pi^2 e^2 \rho_T m_\chi} \int \mathrm{d}q\, q^3 |V(q)|^2 \mathcal{W}(q,\omega) \eta\big(v_{\min}(q,\omega)\big), \tag{S.9}$$

where ρ_T is the mass density of the target, $\eta(v_{\min})$ is the mean inverse DM speed $\int_{v_{\min}} \mathrm{d}^3\mathbf{v}_\chi f(\mathbf{v}_\chi)/v_\chi$, and $v_{\min} = \frac{\omega}{q} + \frac{q}{2m_\chi}$ is the minimum DM speed required to produce an excitation with momentum q and energy ω for DM of mass m_χ. To compare with the literature, we take $f(\mathbf{v}_\chi)$ to be the standard halo model with dispersion $v_0 = 220\,\mathrm{km/s}$, escape velocity $v_{\mathrm{esc}} = 550\,\mathrm{km/s}$, and Earth velocity $v_E = 232\,\mathrm{km/s}$ in the galactic frame. Integrating Eq. (S.9) over ω within the dynamic range of a given experiment gives the total scattering rate.

II. MODELS AND MEASUREMENTS OF THE LOSS FUNCTION

In our formalism, the detector response and its influence on the scattering rate are entirely captured by the complex dielectric function $\epsilon(\mathbf{q},\omega)$ via the loss function $\mathcal{W}$ of Eq. (S.7) and Eq. (2). In principle, this quantity is directly measurable with electromagnetic probes in a given material. However, most measurements presently available in the literature are made at values of $(\mathbf{q},\omega)$ different than those of interest for the detection of light DM (see Fig. 1). Thus, for a first estimate of the scattering rate, we employ analytical approximations to the dielectric function. Important consistency checks can be implemented based on the fact that ϵ^{-1} is defined as a causal correlation function, and thus must have certain analytic properties. In particular, the following two 'sum rule' relations are satisfied exactly by $\mathcal{W}(\mathbf{q},\omega)$ in the limit of an isotropic system [88]:

$$\int_0^\infty \mathrm{d}\omega\, \omega\, \mathcal{W}(\mathbf{q},\omega) = \frac{\pi}{2}\omega_p^2, \tag{S.10}$$

$$\lim_{\mathbf{q}\to 0} \int_0^\infty \mathrm{d}\omega\, \frac{\mathcal{W}(\mathbf{q},\omega)}{\omega} = \frac{\pi}{2}. \tag{S.11}$$

Equation (S.10) is effectively a manifestation of charge conservation, which explains the appearance of the plasma frequency

$$\omega_p^2 = \frac{4\pi\alpha n_e}{m_e}, \tag{S.12}$$

which is proportional to the total electron density n_e in the FEG limit, while Eq. (S.11) follows from causality. Causality also implies that $\mathcal{W}(\mathbf{q},-\omega) = -\mathcal{W}(\mathbf{q},\omega)$ [88], which has important consequences for the projected reach in superconductors, as we will see below.

A. RPA dielectric function for a homogeneous electron gas

An analytic form for the dielectric function of a homogeneous electron gas can be derived from first principles under the random phase approximation (RPA). Here a word about terminology is in order: screening effects arise from Coulomb interactions between electrons, but in RPA these are embodied in the total scalar potential for the system which is solved for self-consistently [88]. Thus RPA captures only a certain subset of electron interactions without including electron-electron interactions directly in the Hamiltonian; in QFT language, it sums the series of ladder diagrams constructed from the 1-loop vacuum polarization to obtain the resummed photon propagator, but does not include higher-loop diagrams involving additional electron lines. This is the sense in which the electrons are treated as 'free' and $\epsilon_{\rm RPA}$ is sometimes referred to as the dielectric function for the free electron gas (FEG). Below we will consider further improvements to this approximation.

The resulting dielectric function at zero temperature is given by Eq. (5.4.21) of Ref. [65] as

$$\epsilon_{\rm RPA}(\mathbf{q},\omega) = 1 + \frac{3\omega_p^2}{q^2 v_F^2}\left\{\frac{1}{2} + \frac{k_F}{4q}\left(1 - \left(\frac{q}{2k_F} - \frac{\omega + i\Gamma_p}{q v_F}\right)^2\right)\mathrm{Log}\left(\frac{\frac{q}{2k_F} - \frac{\omega+i\Gamma_p}{q v_F} + 1}{\frac{q}{2k_F} - \frac{\omega+i\Gamma_p}{q v_F} - 1}\right)\right.$$
$$\left. + \frac{k_F}{4q}\left(1 - \left(\frac{q}{2k_F} + \frac{\omega + i\Gamma_p}{q v_F}\right)^2\right)\mathrm{Log}\left(\frac{\frac{q}{2k_F} + \frac{\omega+i\Gamma_p}{q v_F} + 1}{\frac{q}{2k_F} + \frac{\omega+i\Gamma_p}{q v_F} - 1}\right)\right\}. \quad \text{(S.13)}$$

Here Log denotes the principal value of the natural logarithm, k_F and v_F are the Fermi momentum and Fermi velocity respectively, and Γ_p is a free parameter controlling the width of the plasmon which can also be interpreted as a quasiparticle lifetime. The plasma frequency can also be written in the form

$$\omega_p = \frac{\lambda_{\rm TF} v_F}{\sqrt{3}} = \frac{v_F}{\sqrt{3}}\left[\frac{e}{\pi}\left(2E_F m_e^3\right)^{1/4}\right], \quad \text{(S.14)}$$

where $\lambda_{\rm TF}$ is the (inverse) Thomas–Fermi screening length. We expect the zero-temperature RPA result to be an excellent approximation for $\omega \gg 2\Delta$, where 2Δ is the superconducting gap. As mentioned in the main text, this approximation ignores possible enhancements to the loss function from scattering off of the condensate at energies near or below the gap, which will be considered in future work [67]. In the literature, Eq. (S.13) is known as the Lindhard dielectric function, though Lindhard's formalism may also be applied to semiconductors as well as metals; in what follows, we will use the terms 'Lindhard,' 'RPA,' and 'FEG' interchangeably to refer to Eq. (S.13).

Observe that the arguments of the logarithms in Eq. (S.13) are in general complex. For some values of q and ω, these arguments lie along the negative real axis in the narrow-width limit $\Gamma_p \to 0$, and the imaginary part of ϵ then depends crucially on the choice of branch. The branch choice is fixed by the causality condition $\mathcal{W}(\mathbf{q},-\omega) = -\mathcal{W}(\mathbf{q},\omega)$, which is automatic for positive real values of Γ_p, but the $\Gamma_p \to 0$ limit is non-trivial. The causal result is given by Eq. (5.4.22b) of Ref. [65] as

$$\mathrm{Re}\,\epsilon_{\rm RPA}(\mathbf{q},\omega) \simeq 1 + \frac{\lambda_{\rm TF}^2}{q^2}\left(\frac{1}{2} + \frac{k_F}{4q}\left(1-Q_-^2\right)\log\left|\frac{Q_-+1}{Q_--1}\right| + \frac{k_F}{4q}\left(1-Q_+^2\right)\log\left|\frac{Q_++1}{Q_+-1}\right|\right), \quad \text{(S.15)}$$

$$\mathrm{Im}\,\epsilon_{\rm RPA}(\mathbf{q},\omega) \simeq \frac{3\pi\omega_p^2}{q^3 v_F^2}\begin{cases}\omega/(2v_F) & Q_+ < 1 \\ k_F\left(1-Q_-^2\right)/4 & |Q_-| < 1 < Q_+ \\ 0 & |Q_-| > 1.\end{cases} \quad \text{(S.16)}$$

where $Q_\pm = \frac{q}{2k_F} \pm \frac{\omega}{q v_F}$. The acausal branch prescription was employed in Ref. [6], which as we will see in Section III below, artificially suppresses the scattering rate for low DM masses.

The imaginary part of the Lindhard dielectric function naturally contains the plasmon as a Lorentzian peak at $\omega = \omega_p$ of width Γ_p. For the purposes of light DM detection, kinematics favor energy deposits $\omega \ll \omega_p$. The plasmon has then typically been neglected in the literature in the computation of the scattering rate, *i.e.*, the rate is computed in the limit $\Gamma_p \to 0$. However, for realistic values of Γ_p, the tail of the plasmon peak may significantly contribute to or even dominate the loss function at the relevant values of ω.

For DM–electron scattering in semiconductors, if the deposited energy is $\mathcal{O}(5\,\mathrm{eV})$ or greater, the minimum momentum transfer is $q \gtrsim 5\,\mathrm{keV}$ independent of the DM mass (see Fig. 1 in the main text). Since $k_F \simeq 2\pi/a \simeq 5\,\mathrm{keV}$ for typical interatomic spacings a, this means that the behavior of this part of the spectrum will be determined by the loss function in the region $q \gtrsim k_F$. For these values of q, the DM is probing length scales smaller than the distance between

lattice sites, so we might expect that the inhomogeneities due to the lattice become unimportant and the response is similar to a FEG. For $q > 2k_F$ the loss function peaks when $Q_- \approx 0$, corresponding to $\omega = \frac{q^2 v_F}{2k_F} = \frac{q^2}{2m_e}$, which is elastic scattering from free electrons at rest. For a given q, the loss function is nonzero over a range $\Delta\omega \simeq 2qv_F$ around the peak, reflecting the fact that electrons at the Fermi surface have a nonzero velocity. Note however that the loss function vanishes when $|Q_-| > 1$, which can happen for sufficiently small ω at sufficiently large q. This is an artificial feature of the FEG which is not present in semiconductors, where the valence (and core) electron wavefunctions have a tight-binding character with a momentum-space tail that extends to arbitrarily large values. This regime corresponds to $q \gtrsim Z_{\text{eff}}/a_0 \simeq 15\,\text{keV}$ where a_0 is the Bohr radius and $Z_{\text{eff}} \approx 4$ is the effective nuclear charge felt by the valence electrons in Group 14 elements (carbon, silicon, and germanium). The large-q behavior is especially apparent in some materials like germanium, where the $3d$ shell may become energetically accessible for ω exceeding the binding energy. A corresponding feature is seen in the spectrum in models using tight-binding wavefunctions [4] as well as those using density functional theory (DFT) techniques [3].

B. Plasmon pole approximation and local field corrections

In the limit that the plasmon dominates, the dielectric function may be derived by modeling the atomic response as a damped harmonic oscillator. This is known as the Fröhlich model [89], and the result is

$$\epsilon_{\text{F}}(\mathbf{q},\omega) = \epsilon_c + \frac{\omega_p^2}{(\omega_g^2 - \omega^2) - i\omega\Gamma_p}. \tag{S.17}$$

Here ϵ_c denotes the contribution from core electrons, which is assumed to be independent of $\mathbf{q}$ and ω, and ω_g is an average band gap which can be set to zero for metals. The corresponding loss function features a Breit–Wigner-like peak, with the form

$$\mathcal{W}_{\text{F}}(\mathbf{q},\omega) = \frac{\omega_p^2 \omega \Gamma_p}{\epsilon_c^2 \left(\omega_g^2 + \omega_p^2/\epsilon_c^2 - \omega^2\right)^2 + \omega^2\Gamma_p^2}. \tag{S.18}$$

This function satisfies the sum rules of Eqs. (S.10) and (S.11) with $\epsilon_c = 1$ and $\omega_g = 0$. Note that this form of the loss function is linear in ω for $\omega \ll \omega_p$.

The low-energy loss function is also subject to effects which are not included in the Lindhard dielectric function. Ref. [60] (hereafter denoted 'GSRF') fits the plasmon in aluminum including a local-field correction and accounting for the polarizability of atomic cores χ_{core}, resulting in a dielectric function of the form

$$\epsilon_{\text{G}}(\mathbf{q},\omega) = 1 + \frac{[\omega + i\Gamma_p(\mathbf{q})]\,[\epsilon_{\text{RPA}}(\mathbf{q},\omega) - 1 + 4\pi\chi_{\text{core}}]}{\omega\,(1 - G(\mathbf{q})\,[\epsilon_{\text{RPA}}(\mathbf{q},\omega) - 1]) + i\Gamma_p(\mathbf{q})\,(1 - G(\mathbf{q})\,[\epsilon_{\text{RPA}}(\mathbf{q},0) - 1])\,\frac{\epsilon_{\text{RPA}}(\mathbf{q},\omega)-1+4\pi\chi_{\text{core}}}{\epsilon_{\text{RPA}}(\mathbf{q},0)-1+4\pi\chi_{\text{core}}}}, \tag{S.19}$$

where $G(\mathbf{q})$ is known as the exchange parameter and arises in the microscopic theory from 1-loop corrections to the electron-photon vertex [88]. Ref. [60] provides fits to G and Γ_p as functions of $\mathbf{q}$. Complex values of G produce damping, which influences the form of the loss function at small values of ω. However, $\text{Im}\,G(\mathbf{q}) \neq 0$ can lead to unphysical negative values of the loss function at the smallest values of ω, thereby violating the positivity requirements imposed by the sum rules, and moreover G as computed in various microscopic theories tends to be real [88]. Following Ref. [60], we divide our treatment into two cases, one with complex-valued G ('damped') and one with real-valued G ('undamped').

C. Dielectric function for Dirac materials

Dirac materials are characterized by electrons with the approximately linear dispersion characteristic of relativistic Dirac fermions, rather than the usual quadratic dispersion expected at a band minimum. In real materials, there are typically two such bands, one below and one above the Fermi energy, with dispersions $E_\pm(\mathbf{k}) = \pm\sqrt{v_F^2\mathbf{k}^2 + \Delta^2}$. Here, Δ plays the role of the fermion mass and the Fermi velocity v_F is the analogue of the speed of light; the gap at the Dirac point with $\mathbf{k} = 0$ is 2Δ. The band structure may be anisotropic, with different Fermi velocities along different lattice directions, but for pedagogical purposes we will focus here on isotropic materials; see Refs. [27, 28]

for a detailed investigation of anisotropic Dirac materials for DM detection.

In the approximation that only two nondegenerate bands contribute to the Dirac electron spectrum, the dielectric function may be computed using Lindhard's formalism in the Bloch wave basis [65]. At zero temperature, with the valence (−) band full and the conduction (+) band empty, this reads

$$\epsilon_{\rm Dirac}(\mathbf{q},\omega) = 1 + \lim_{\eta\to 0}\frac{1}{V}\frac{e^2}{q^2}\int_{\rm BZ}\frac{V_{\rm uc}\mathrm{d}^3\mathbf{k}}{(2\pi)^3}\frac{2}{E_+(\mathbf{k}+\mathbf{q}) - E_-(\mathbf{k}) - \omega - i\eta}\left|\langle \mathbf{k}+\mathbf{q};+|e^{i\mathbf{q}\cdot\mathbf{r}}|\mathbf{k};-\rangle\right|^2, \tag{S.20}$$

where $|\mathbf{k};\pm\rangle$ represents a Bloch wavefunction with crystal momentum $\mathbf{k}$ in the band $-$ or $+$, V is the crystal volume, the factor of 2 is for spin degeneracy, and the integral is taken over the first Brillouin zone (BZ) in the continuum limit using the unit cell volume to regularize the momentum sum, $\sum_{\mathbf{k}} \to \int V_{\rm uc}\,\mathrm{d}^3\mathbf{k}/(2\pi)^3$. There are some complications with this procedure in the case of anisotropic materials [27], but it yields an accurate estimate for the imaginary part in isotropic materials, which is dominated by the smallest gaps and hence the bands other than the Dirac bands may be neglected. However, as noted in Ref. [27], $\mathrm{Re}[\epsilon(0,0)]$ acts as a background dielectric constant receiving contributions from the entire BZ and thus cannot be reliably calculated analytically. We may therefore estimate the real part as simply $\mathrm{Re}(\epsilon_{\rm Dirac}) = \kappa \gg 1$ independent of $\mathbf{q}$ and ω over the relevant kinematic range.

To obtain the imaginary part, we may use the identity $\mathrm{Im}(\lim_{\eta\to 0}\frac{1}{x-i\eta}) = \pi\delta(x)$ and perform the integral using spinor wavefunctions with the matrix element given in Ref. [16]. Note that this is precisely analogous to performing the phase space integral over the valence and conduction bands in the single-particle formalism for determining the scattering rate; the dielectric function allows us to express the results of Ref. [16] in a more convenient and generalizable formalism. Equivalently, we may recognize that with the replacements $\Delta \to m_e$ and $v_F \to c$, the imaginary part is identical to that of the 1-loop vacuum polarization in relativistic quantum electrodynamics (QED), which is proportional to the cross section for $\gamma^* \to e^+e^-$ by the optical theorem [90]. The result is

$$\mathrm{Im}\,\epsilon_{\rm Dirac}(q,\omega) = \frac{e^2}{12\pi v_F}\sqrt{1-\frac{4\Delta^2}{\omega^2 - v_F^2q^2}}\left(1+\frac{2\Delta^2}{\omega^2-v_F^2q^2}\right)\Theta(\omega^2 - v_F^2q^2 - 4\Delta^2), \tag{S.21}$$

where the coefficient $e^2/(12\pi)$ is (up to a factor of π) the familiar 1-loop beta function coefficient of QED. Indeed, the physics of the dielectric function is the same in Dirac materials as it is in the true QED vacuum; the screening of bare charges due to $\mathrm{Im}(\epsilon)$ at $q \simeq 2m_e$ is known as the Uehling potential.

As long as v_F is not too small, $\mathrm{Im}(\epsilon) \lesssim 1$. (Otherwise perturbation theory would break down, as noted in Ref. [16].) Then if $\kappa \gg 1$, we may approximate $\mathrm{Im}(-1/\epsilon) \approx \mathrm{Im}(\epsilon)/\kappa^2$ and thus

$$\mathcal{W}_{\rm Dirac}(q,\omega) = \frac{e^2}{12\kappa^2\pi v_F}\sqrt{1-\frac{4\Delta^2}{\omega^2 - v_F^2q^2}}\left(1+\frac{2\Delta^2}{\omega^2-v_F^2q^2}\right)\Theta(\omega^2 - v_F^2q^2 - 4\Delta^2)\Theta(\omega_{\rm max}-\omega) \tag{S.22}$$

Setting $\Delta = 0$ gives Eq. (4) in the main text. The last factor may be explained as follows. In real materials, the Dirac band structure does not extend throughout the entire BZ, but deviates from linearity at some point. In Ref. [16] this was expressed as a momentum cutoff Λ, which is required to regularize the real part of $\epsilon_{\rm Dirac}$. Here, since we are dealing with model functions rather than real materials, we instead impose a cutoff $\omega_{\rm max}$ on the depth of the Dirac band, which has typical values of $\omega_{\rm max} \simeq 0.5\,\mathrm{eV}$ in *e.g.* $ZrTe_5$ [16]. Finally, note that $\mathcal{W}_{\rm Dirac}$ violates the causality requirement $\mathcal{W}_{\rm Dirac}(q,-\omega) = -\mathcal{W}_{\rm Dirac}(q,\omega)$. This indicates that $\mathcal{W}_{\rm Dirac}$ as computed here does not represent the entire loss function, and in particular (as noted in the main text) it is missing plasmon contributions.

D. Measurements of the loss function in various materials

Measurements of the loss function in the vicinity of the plasmon peak are available in the literature for certain materials, so it is already possible to fit the Fröhlich model directly to data and to assess the significance of the plasmon tail at $\omega \ll \omega_p$. Figure S1 (left) shows such a fit to measurements in Al. While the fit is excellent in the vicinity of the plasmon peak, the behavior at $\omega \ll \omega_p$ should be viewed only as a benchmark: other physical effects contribute at these energies, notably those encapsulated by the Lindhard dielectric function which incorporates electron screening effects. See Fig. S4 and Section III below for further details.

High-precision measurements of the loss function at nonzero q have also been performed for Si using X-ray scattering [69]. The plasmon is clearly visible at small q, but here we focus on the behavior at large q. Figure S1 (center) shows the measured loss function along the [100] crystal direction (solid lines), compared to the RPA loss function

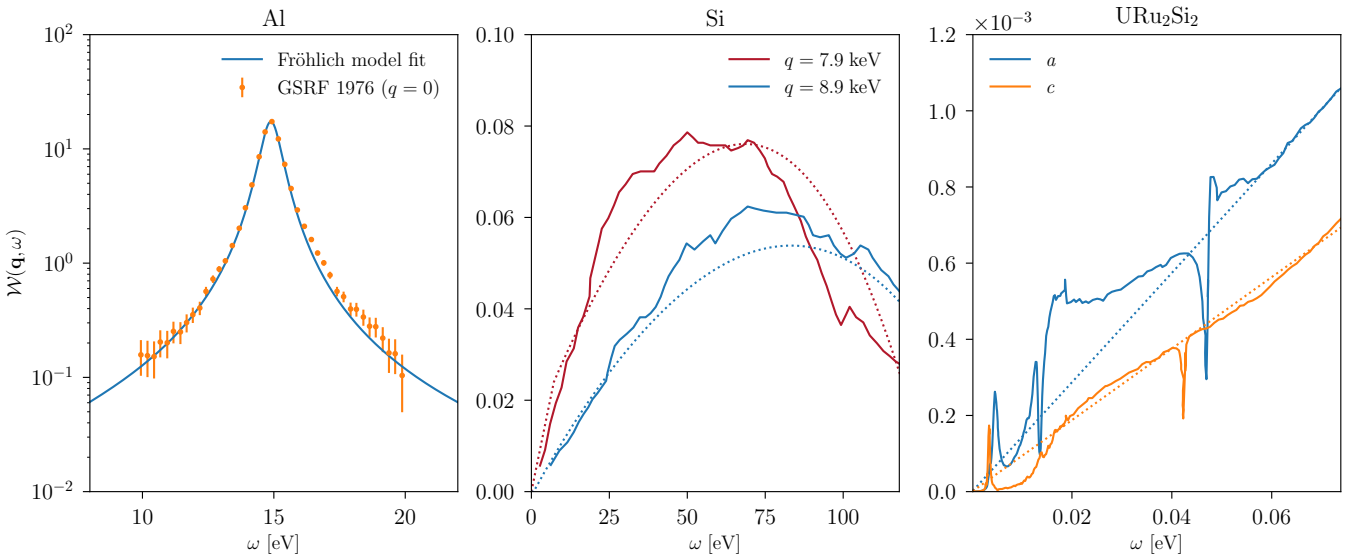

FIG. S1. Measurements of the loss function $\mathcal{W}(\mathbf{q}, \omega) = \mathrm{Im}(-1/\epsilon(\mathbf{q}, \omega))$ in Al, Si, and URu_2Si_2 along with model fits when appropriate. **Left:** loss function for Al at $q = 0$ in the vicinity of the plasmon peak from Ref. [60], fit with the Fröhlich model of Eq. (S.18). The best-fit parameters are $(\omega_p, \Gamma_p) = (14.9\,\mathrm{eV},\ 0.863\,\mathrm{eV})$. Error bars indicate the accuracy with which the data points could be transcribed from Ref. [60]. **Center:** loss function for Si at large momenta $q > 2\pi/a$, measured from X-ray scattering in Ref. [69]. Dashed lines show the Lindhard RPA loss function with $\Gamma_p = 0$, $k_F = m_e v_F$, and $\omega_p = 16.67\,\mathrm{eV}$ [71]. The Fermi velocity is treated as a free parameter and is fixed here to the best-fit value of $v_F = 2.59 \times 10^8\,\mathrm{cm/s} = 8.6 \times 10^{-3}$ in natural units, which is comparable to Fermi velocities of metals with similar densities. **Right:** loss function in URu_2Si_2 at $q = 0$ measured along two different crystal axes a and c at $T = 9\,\mathrm{K}$ [61] (solid), along with a linear fit to both datasets (dashed). If interpreted as the tail of a valence electron plasmon, the slope should be Γ_p/ω_p^2. The fit gives a slope of $\Gamma_p/\omega_p^2 \simeq 14\ (9) \times 10^{-3}\,\mathrm{eV}^{-1}$ along the a (c) axis which implies $\Gamma_p/\omega_p \simeq 0.21\ (0.13)$ for $\omega_p \simeq 15\,\mathrm{eV}$, values which are typical for other metals.

for the homogeneous electron gas taking $\omega_p = 16.67\,\mathrm{eV}$ for the measured plasmon frequency [71]. While semiconductors and insulators do not, strictly speaking, have a Fermi velocity at zero temperature where there are no free carriers, we may regard v_F as a tuneable parameter which governs the behavior of the loss function at small ω. With $v_F = 8.6 \times 10^{-3}$, on the same scale as v_F for typical metals, the fit is quite good, especially for $\omega < 25\,\mathrm{eV}$. On the other hand, at $q = 10\,\mathrm{keV}$, the RPA loss function vanishes identically for $\omega < 12\,\mathrm{eV}$, which is likely unphysical given that atomic tight-binding wavefunctions have support in this kinematic range. The purpose of this comparison is not to advocate for using this extremely simplified model—indeed, data should be used to compute DM rates whenever possible—but rather to demonstrate how in the absence of data a simple model may provide an accurate estimate for the light-mediator spectrum for $\omega \in [5\,\mathrm{eV}, 10\,\mathrm{eV}]$, where the rate integral is dominated by $q \in [5\,\mathrm{keV}, 10\,\mathrm{keV}]$. Indeed, the success of the RPA model suggests that this part of the spectrum from scattering in any semiconductor or insulator with eV-scale bandgaps is nearly universal, determined only by the valence electron density and an effective Fermi velocity. This model may be seen as an extension, accounting for screening, of earlier simplified models for scattering in semiconductors using atomic orbitals or tight-binding wavefunctions [2, 4].

To complete our survey of sample loss functions, we show in Fig. S1 (right) the measured loss function at $q = 0$ for URu_2Si_2 along the a and c crystal axes, measured with Fourier transform infrared spectrometry [61]. URu_2Si_2 has been extensively studied for decades [91] due to its unusual 'hidden order' below 17.5 K, and thus has been synthesized as ultra-pure single crystals. Below $T_c = 1.5\,\mathrm{K}$ it behaves as a conventional superconductor [92]. A number of features are present below 20 meV which may be interpreted as heavy-fermion plasmons, as we discuss in the main text. Based on this interpretation, to perform our rate estimates in the main text, we extrapolate the loss function as independent of q out to $q = q_c \simeq 100\,\mathrm{eV}$. Indeed, this is the standard approximation made in scattering experiments near the plasmon pole [71]. Then, we see from Eq. (S.9) that the spectrum is largely determined by the shape of the zero-momentum loss function $\mathcal{W}(\omega)$, with the inverse mean speed η only serving to enforce the kinematic condition $q > \omega/v_\chi$. All of the approximations we have made may easily be dropped once momentum-resolved data on $\mathcal{W}(\mathbf{q}, \omega)$ within the DM regions shown in Fig. 1 is available.

It is also interesting to note that at larger ω, the loss function is linear to an excellent approximation, in the c direction above 20 meV and in the a direction above 50 meV. In Fig. S1 we show a linear fit to both loss functions

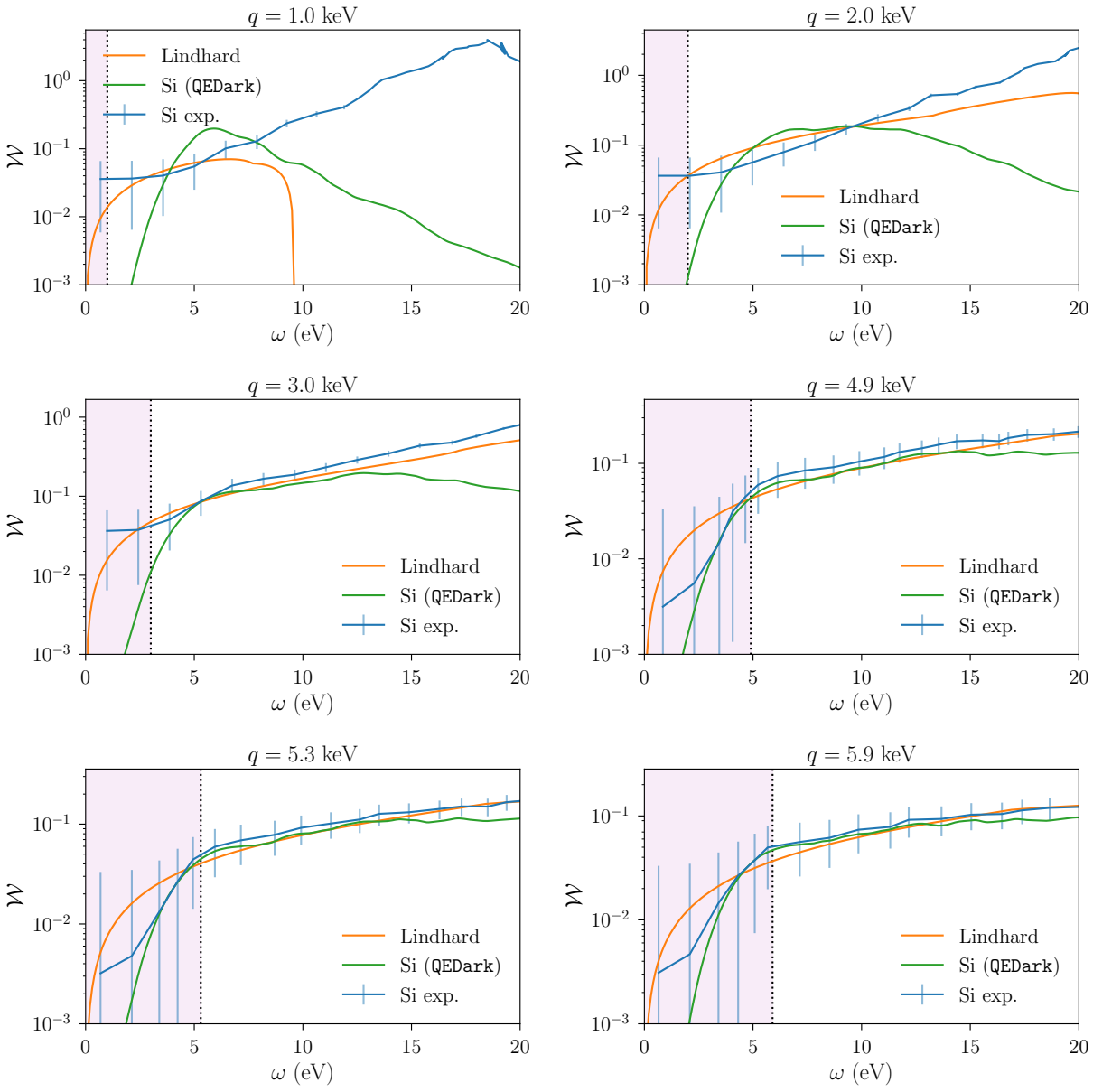

FIG. S2. Loss function comparisons in Si for various q, as a function of ω. Error bars indicate the accuracy with which the data points could be transcribed from Ref. [69]. The shaded purple region represents the kinematically-allowed region for $v_\chi = 10^{-3}$. The measured loss function agrees fairly well with both the loss function computed from the single-particle basis from `QEdark` [3] and the Lindhard FEG approximation in the range 5–10 eV for ω, but there are large differences at both small ω near the gap, and near the plasmon energy $\omega_p \simeq 17\,\text{eV}$ for small q.

with zero offset. In the Fröhlich model Eq. (S.18), the plasmon tail gives a loss function $\mathcal{W}_F(q=0,\omega) \approx \omega \times (\Gamma_p/\omega_p^2)$ at small ω. The slope of the linear fit is consistent with $\Gamma_p/\omega_p \simeq 0.1 - 0.2$ and $\omega_p \simeq 15\,\text{eV}$, which would be reasonable parameters for the ordinary valence electron plasmon in a generic metal. This data therefore provides some preliminary indication that the linear tail of the plasmon in ordinary superconductors like Al may extend down to the meV scale. We emphasize again that dedicated measurements are needed to confirm this.

E. Semiconductor spectrum in the free-electron gas approximation

In order to relate the energy loss function to the crystal form factor [3, 25], we compare

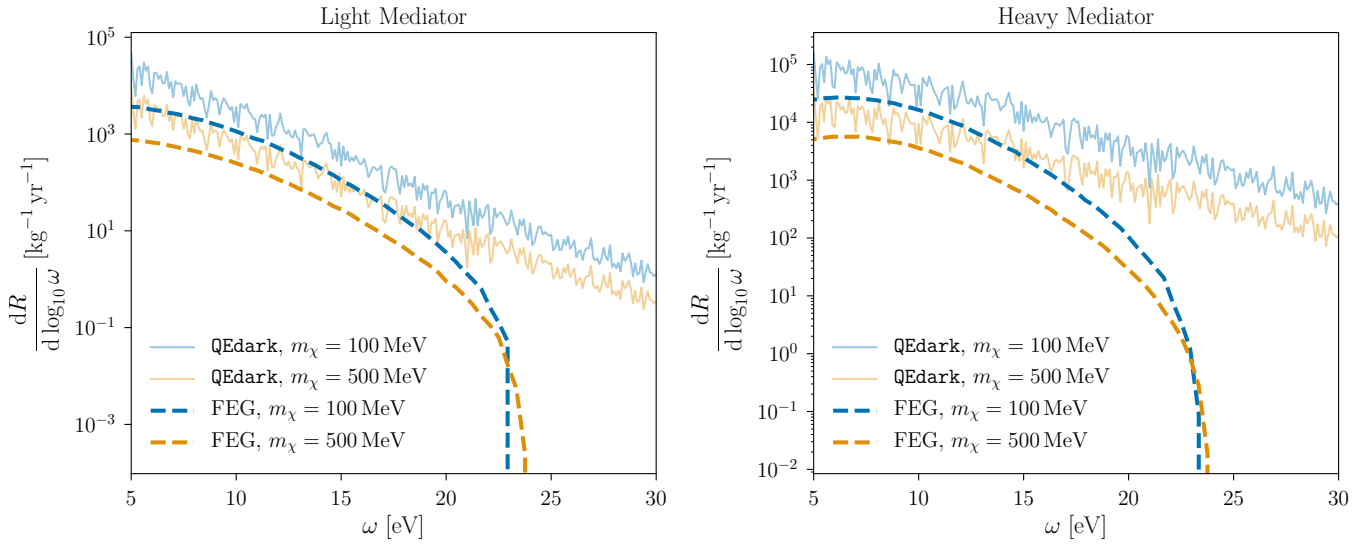

FIG. S3. Recoil spectra in Si at fixed $\overline{\sigma}_e = 10^{-37}\,\mathrm{cm}^2$, for light and heavy mediators (scalar or vector). Solid curves are computed with `QEdark` [3]. Dashed curves are computed from Eq. (1) with the Lindhard RPA loss function, Eq. (S.13) with $v_F = 8.6 \times 10^{-3}$, $k_F = m_e v_F$, and $\omega_p = 16.67\,\mathrm{eV}$.

$$\Gamma(\mathbf{v}_\chi) = \int \frac{\mathrm{d}^3\mathbf{q}}{(2\pi)^3} |V(q)|^2\, \mathcal{S}(\mathbf{q},\omega) \tag{S.23}$$

to Eq. (1), which gives the relation between the dynamic structure factor $\mathcal{S}(\mathbf{q},\omega)$ defined in Ref. [25] and the loss function via

$$\mathcal{S}(\mathbf{q},\omega) = \frac{2q^2}{e^2}\mathcal{W}(\mathbf{q},\omega). \tag{S.24}$$

On the other hand, the dynamic structure factor in a semiconductor, computed in the basis of single-particle states, can be related to the crystal form factors $|f_{ii'\mathbf{k}\mathbf{k}'\mathbf{G}}|^2$ via [3, 25]

$$\mathcal{S}(\mathbf{q},\omega) = 2\sum_{i,i',\mathbf{G}} \int_{\mathrm{BZ}} \frac{d^3\mathbf{k}}{(2\pi)^3}\frac{d^3\mathbf{k}'}{(2\pi)^3} 2\pi\delta(E_{i'\mathbf{k}'} - E_{i\mathbf{k}} - \omega) 2\pi\delta(|\mathbf{k}' - \mathbf{k} + \mathbf{G}| - q)|f_{ii'\mathbf{k}\mathbf{k}'\mathbf{G}}|^2, \tag{S.25}$$

where the momentum integral is taken over the first BZ, $\mathbf{G}$ runs over all reciprocal lattice vectors, and i and i' run over all valence and conduction bands, respectively. Thus we can compute an equivalent loss function from `QEdark` [3] crystal form factors by

$$\mathcal{W}(\mathbf{q},\omega) = \frac{e^2}{q^2}\sum_{i,i',\mathbf{G}} \int_{\mathrm{BZ}} \frac{d^3\mathbf{k}}{(2\pi)^3}\frac{d^3\mathbf{k}'}{(2\pi)^3} 2\pi\delta(E_{i'\mathbf{k}'} - E_{i\mathbf{k}} - \omega) 2\pi\delta(|\mathbf{k}' - \mathbf{k} + \mathbf{G}| - q)|f_{ii'\mathbf{k}\mathbf{k}'\mathbf{G}}|^2 \tag{S.26}$$

Using Eq. (S.26), we can compare the measured loss function to the loss function computed in the single-particle basis by `QEdark`, as well as the Lindhard dielectric function for the FEG with the best-fit v_F in Fig. S1. The results are shown in Fig. S2. Note that for a given q, the range of ω which is accessible is $\omega < qv_\chi$, which only comprises a small piece of the total support of $\mathcal{W}(\mathbf{q},\omega)$. Regardless, we see that `QEdark` tends to slightly underpredict the measured loss in the kinematically-allowed region. Furthermore, `QEdark` accurately reproduces the measured loss in the near-gap region $\omega \in [1\,\mathrm{eV}, 5\,\mathrm{eV}]$ where Lindhard fails to do so, as expected. On the other hand, `QEdark` fails to capture the plasmon which is seen in the measured loss function because the single-particle band structure states do

not account for collective effects.

Overall, though, the nearly-linear shape of the measured loss function in the range $\omega \in [5\,\mathrm{eV}, 15\,\mathrm{eV}]$ is reproduced fairly well by the Lindhard model, and matches that of `QEdark`. We therefore expect that the spectral shape (though perhaps not the normalization) will be captured in this energy range by the simple Lindhard model for the loss function. Moreover, since the Lindhard model loss function goes to zero at sufficiently large q for small ω, and since the rate recieves contributions from *all* $q > \omega/v_\chi$, we expect the Lindhard approximation to be best for a light mediator which weights the rate integrand by $|V(q)|^2 \propto 1/q^4$. The results are shown in Fig. S3. Indeed, the Lindhard FEG model matches the spectrum fairly well for the light mediator, roughly independent of the DM mass as long as the DM kinetic energy is well above the gap. The spectrum for a heavy mediator is a poorer match, especially at large ω where the kinematic mismatch between the FEG and the bound atomic wavefunctions becomes more important. We emphasize once again that these simple arguments are *not* meant to replace a measurement of $\mathcal{W}$ in the relevant kinematic range, which would predict the spectrum unambiguously. However, they do highlight a qualitative understanding of the spectrum in a limited energy range based on simple material properties like the effective v_F, which may be useful for identifying other detector materials suitable for DM-electron scattering. Furthermore, the part of the spectrum where the FEG model performs best corresponds to the 2-electron bin in Si, which is of considerable practical importance to experiments: the 1-electron bin is typically dominated by backgrounds such as leakage current and Cherenkov radiation [37], while the rates in the bins with 3 or more electrons drop precipitously, at least based on estimates from the single-particle loss function. Integrating the FEG spectra from a threshold of $\omega = 4.7$ eV, corresponding to a $2e^-$ threshold in the model of Ref. [3], we obtain the reach curve shown in Fig. 2 in the main text.

III. UPDATED REACH PROJECTIONS FOR SUPERCONDUCTORS

In Ref. [5], the scattering rate in a superconductor is first computed treating the electrons as free particles, with screening included afterwards in Ref. [6] via a correction to the matrix element. We now show that the result of Ref. [6] at $T = 0$ is exactly reproduced by our Eq. (1) when $\epsilon(\mathbf{q}, \omega)$ is taken to be the Lindhard dielectric function in the limit of vanishing plasmon width.

In a relativistic formalism for single-particle scattering, the superconductor scattering rate is given by

$$\Gamma(\mathbf{v}_\chi) = \int \frac{\mathrm{d}^3\mathbf{p}'_\chi}{(2\pi)^3} \frac{\langle|\mathcal{M}|^2\rangle}{16 E_\chi E'_\chi E_e E'_e} \frac{S(\mathbf{q},\omega)}{|\epsilon(\mathbf{q},\omega)|^2}, \tag{S.27}$$

where $\mathbf{q} \equiv \mathbf{p}_\chi - \mathbf{p}'_\chi$ denotes the 3-momentum transfer, $\mathbf{p}'_\chi$ denotes the momentum of the scattered dark matter particle in the final state, and $S(\mathbf{q}, \omega)$ (not to be confused with the dynamic structure factor defined in Eq. (S.24) above) characterizes the available phase space, to be defined shortly. The presence of $|\epsilon|^2$ in the denominator of Eq. (S.27) accounts for screening and was treated in Ref. [6] as an in-medium modification to the dark photon propagator. In the non-relativistic limit, any interaction of the class considered in Eq. (S.8) gives rise to a matrix element of the form

$$\frac{\langle|\mathcal{M}|^2\rangle}{16 E_\chi E'_\chi E_e E'_e} \simeq \left(\frac{g_\chi g_e}{q^2 + m^2_{\phi,V}}\right)^2 = |V(q)|^2, \tag{S.28}$$

where $q = |\mathbf{q}|$. Equation (S.27) is trivially transformed to an integral over $\mathbf{q}$, and the rate becomes

$$\Gamma(\mathbf{v}_\chi) = \int \frac{\mathrm{d}^3\mathbf{q}}{(2\pi)^3} |V(q)|^2 \frac{S(\mathbf{q},\omega)}{|\epsilon(\mathbf{q},\omega)|^2}. \tag{S.29}$$

Thus, to agree with Eq. (1), it is sufficient to have

$$S(\mathbf{q},\omega) = \frac{2q^2}{e^2} \operatorname{Im} \epsilon(\mathbf{q},\omega). \tag{S.30}$$

Equation (S.30) holds exactly in the low-temperature limit for the form of S used in Refs. [5, 6], where the superconductor is treated as a free electron gas. In this case, S is given by

$$S(\mathbf{q},\omega) = 2 \int \frac{\mathrm{d}^3\mathbf{p}_e}{(2\pi)^3} \frac{\mathrm{d}^3\mathbf{p}'_e}{(2\pi)^3} (2\pi)^4 \delta^4(P_\chi + P_e - P'_\chi - P'_e) f_{\mathrm{FD}}(E_e) \left[1 - f_{\mathrm{FD}}(E'_e)\right], \tag{S.31}$$

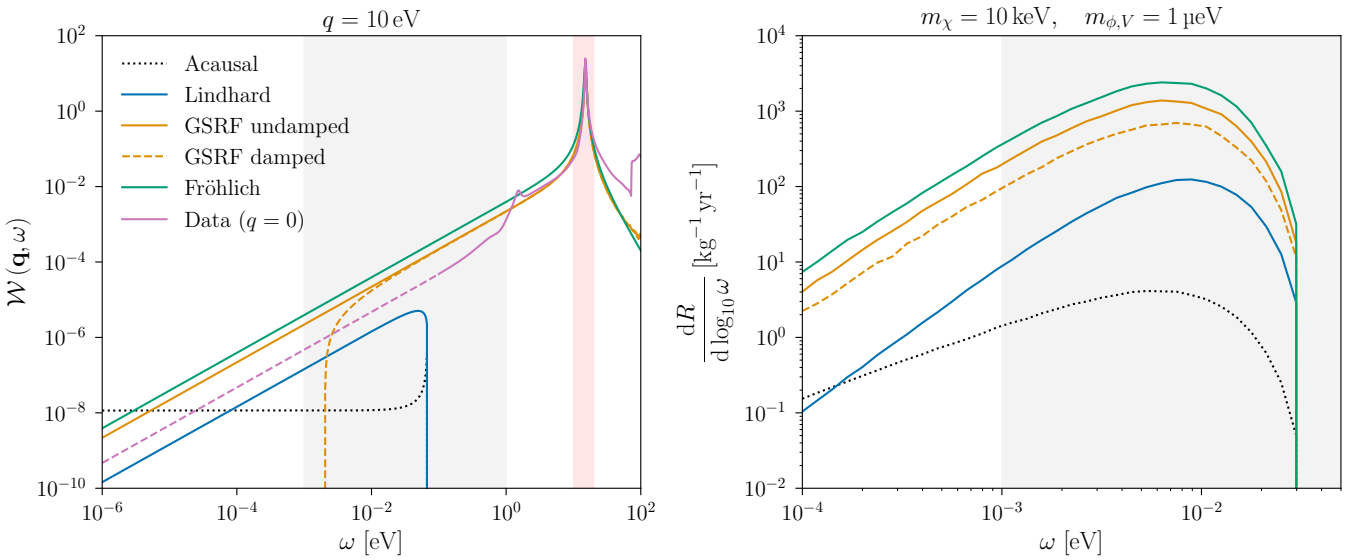

FIG. S4. **Left:** loss function for each of several models for Al, for $q = 10\,\mathrm{eV}$. The curve labeled 'Acausal' shows the loss function used in [6], which involves an unphysical choice of branch cut in the complex logarithm. The Fröhlich model fit is the same as that shown in Fig. S1, for which measured data are only available within the red band. The Lindhard model is the RPA dielectric function Eq. (S.13) with $\Gamma_p = 0$, and the GSRF models use fit parameters for Eq. (S.19) from Ref. [60], with 'undamped' corresponding to $\mathrm{Im}\, G = 0$ and 'damped' corresponding to $\mathrm{Im}\, G \neq 0$. The damped curve becomes negative at small ω, which is an unphysical consequence of the GSRF model. The curve labeled 'Data' shows the fit to $q = 0$ measurements provided by Ref. [66]. We use dashes to indicate the continuation of the fit beyond the range of measured data. The gray band shows the reference range of 1 meV–1 eV deposits. **Right:** recoil spectra corresponding to each of these loss functions, assuming $(m_\chi,\, m_{\phi,V}) = (10\,\mathrm{keV},\, 1\,\mu\mathrm{eV})$ and $\overline{\sigma}_e = 10^{-39}\,\mathrm{cm}^2$.

where f_{FD} is the Fermi–Dirac distribution and the P_i denote 4-momenta. We reserve p_i for the magnitudes of 3-momenta. The integration over $\mathbf{p}'_e$ is readily performed using the 3-momentum delta function. Writing the $\mathbf{p}_e$ integral in spherical coordinates and performing the trivial integral over the azimuthal angle produces

$$S(\mathbf{q}, \omega) = 2 \int \frac{p_e^2\, \mathrm{d}p_e\, \mathrm{d}(\cos\theta)}{(2\pi)^2} \delta\left(\omega - \frac{q^2 + 2p_e q \cos\theta}{2m_e}\right) f_{\mathrm{FD}}(E_e)\left[1 - f_{\mathrm{FD}}(E'_e)\right], \tag{S.32}$$

where θ denotes the angle between $\mathbf{p}_e$ and $\mathbf{q}$. The remaining delta function can be used to evaluate the integral over $\cos\theta$, but here care must be taken to enforce $|\cos\theta| \leq 1$. With the appropriate Heaviside function, the final integral becomes

$$S(\mathbf{q}, \omega) = \int \mathrm{d}p_e\, \frac{m_e p_e}{\pi q}\left[1 - f_{\mathrm{FD}}(E'_e)\right] \Theta\left(1 - \left|\frac{2m_e\omega - q^2}{2p_e q}\right|\right). \tag{S.33}$$

Now the zero-temperature Fermi–Dirac distribution can be inserted and the integral can be performed analytically. The result is

$$S(\mathbf{q}, \omega) = \frac{m_e^2}{\pi q} \begin{cases} \omega & 0 < \omega < |E_-| \\ E_F - \frac{(E_q - \omega)^2}{4E_q} & |E_-| < \omega < E_+ \\ 0 & \text{otherwise,} \end{cases} \tag{S.34}$$

where $E_q \equiv q^2/2m_e$ and $E_\pm = E_q \pm q v_F$. The conditions in Eq. (S.34) are equivalent to those in Eq. (S.16), *i.e.*, the imaginary part of the Lindhard dielectric function in the limit that the plasmon is infinitely long-lived. Equation (S.30) follows by direct comparison.

Given this agreement between the single-particle and dielectric-function formalisms, Eq. (1) can reproduce prior calculations of the scattering rate in superconductors; essentially, the final-state phase space integral is pre-computed in $\mathrm{Im}(\epsilon)$. However, Eq. (1) is more flexible than the traditional calculation in that we are not limited to the narrow-plasmon limit of the Lindhard dielectric function. Any model or measurement of the loss function can be inserted

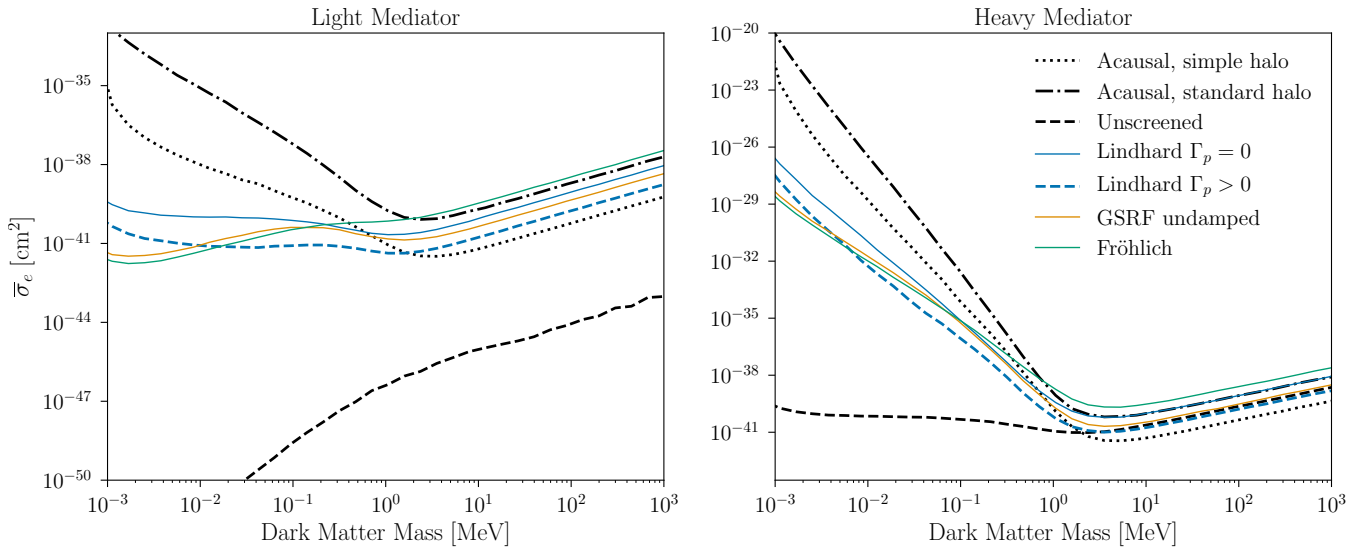

FIG. S5. Projected reach for an aluminum superconductor target for several forms of the loss function for scalar or vector mediators. The dotted curve is computed with the simple halo model ($v_E = 0$, $v_{\rm esc} = 500\,{\rm km/s}$), and all others assume the standard halo model. The dashed line ('unscreened') is computed in the single-particle formalism with no correction for screening, *i.e.*, without the factor of $|\epsilon|^2$ in the denominator of Eq. (S.27); this is unphysical for any spin-independent DM-electron interaction.

directly in Eq. (1).

To evaluate the event rate in a superconducting detector, we take the velocity of the DM in the galactic frame to have a modified Maxwell–Boltzmann distribution,

$$f(\mathbf{v}_\chi) \propto \exp\left(-\mathbf{v}_\chi^2/v_0^2\right)\Theta\left(v_{\rm esc} - |\mathbf{v}_\chi|\right). \tag{S.35}$$

For our reach projections, we take $v_0 = 220\,{\rm km/s}$ and $v_{\rm esc} = 550\,{\rm km/s}$, and we take Earth to have a velocity $v_E = 232\,{\rm km/s}$ in the galactic frame. This matches the conventions of Ref. [16]. In order to facilitate comparison with other results in the literature, we also show some results with $v_E = 0$ and $v_{\rm esc} = 500\,{\rm km/s}$, matching the conventions of *e.g.* Refs. [5, 6]. We refer to this as the 'simple halo' scenario. Finally, for illustrative purposes, we show selected results for a hypothetical halo with $v_0 = v_{\rm esc} = 10^4\,{\rm km/s}$ and $v_E = 0$. In this 'fast DM' scenario, the plasmon peak is kinematically accessible, and this is directly visible as a feature in the recoil spectrum.

The various models for the loss functions in Al are shown in Fig. S4, together with the corresponding DM recoil spectra for a kg-yr exposure. The undamped GSRF model and the Lindhard model with $\Gamma_p = 0$ correspond to the boundaries of the shaded region in Fig. 2. We also show the result obtained by choosing the acausal branch in the Lindhard dielectric function. It is clear from Fig. S4 that at low energies, a naive extrapolation of the plasmon tail dominates over the Lindhard loss function with its infinitely long-lived plasmon. Moreover, the energy range of interest for light DM detection is precisely where the effects of damping in the GSRF loss function become important. While the loss functions given here are valuable benchmarks, the true loss function likely falls somewhere between the Lindhard result and the plasmon tail. This is also suggested by fitting the measurements of Ref. [66], which go down to $\omega = 100\,{\rm meV}$ and lie somewhat below the plasmon tail. (See the purple line in Fig. S4.) To accurately predict the DM scattering rate, it is both essential and feasible to *measure* the loss function in the entire relevant regime of $1\,{\rm meV} < \omega < 1\,{\rm eV}$.

Figure S5 shows updated reach curves for an aluminum superconductor target alongside the results of Refs. [5, 6]. The reach curves are specified with respect to a reference cross section defined by

$$\overline{\sigma}_e = \frac{16\pi\mu_{e\chi}^2\alpha_e\alpha_\chi}{\left((\alpha_{\rm EM}m_e)^2 + m_\phi^2\right)^2}, \tag{S.36}$$

where $\mu_{\chi e}$ denotes the reduced mass of the electron–DM system, m_ϕ is the mediator mass, and $\alpha_{e,\chi} = g_{e,\chi}^2/(4\pi)$ in terms of the couplings which define the potential in Eq. (S.8). In Fig. S5, 'light mediator' means $m_\phi \ll \alpha_{\rm EM}m_e$

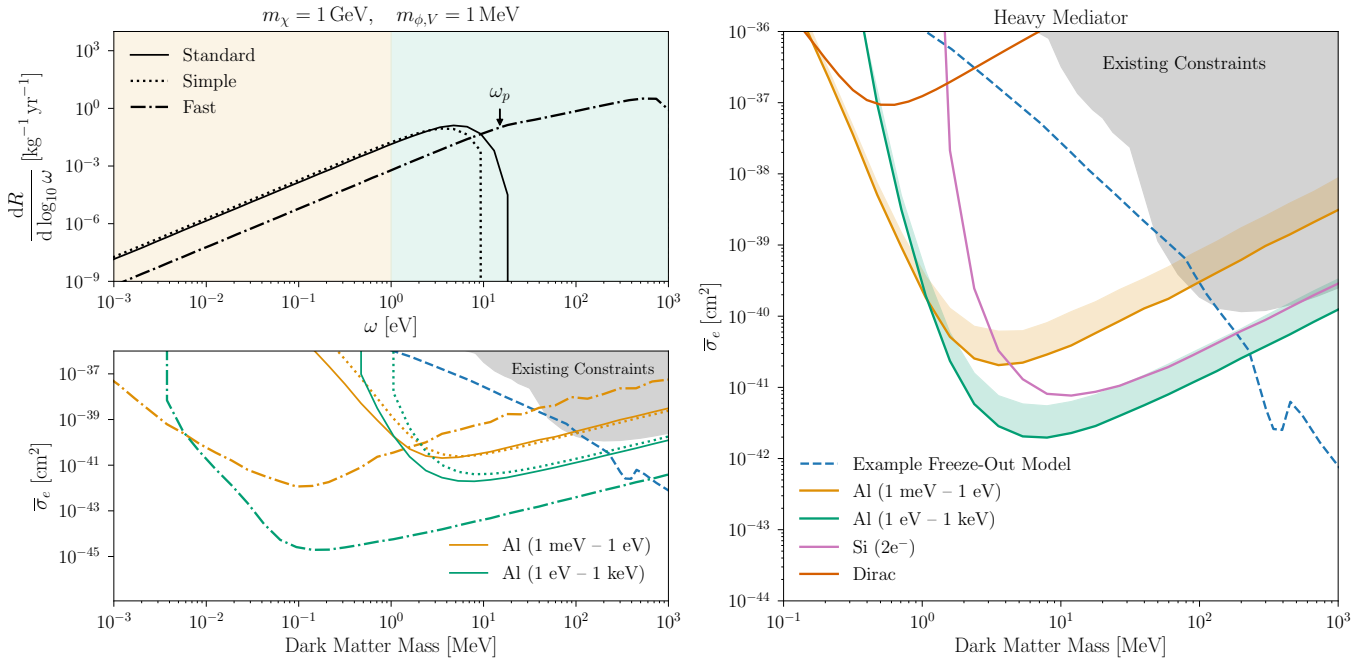

FIG. S6. **Top left:** recoil spectra in an Al superconductor for $(m_\chi, m_\phi) = (1\,\mathrm{GeV}, 1\,\mathrm{MeV})$ and $\overline{\sigma}_e = 10^{-42}\,\mathrm{cm}^2$ assuming the GSRF loss function without damping for several DM velocity distributions. See text for details. The fast halo scenario is unrealistic and is shown for illustrative purposes only: in this case, the plasmon peak is kinematically accessible, and the recoil spectrum exhibits a corresponding kink at $\omega = \omega_p$. The shaded areas indicate two fiducial experimental configurations, one sensitive to deposits 1 meV–1 eV (orange), and the other sensitive to deposits 1 eV–1 keV (green). **Bottom left:** projected reach in an Al superconductor for a 1 kg-yr exposure assuming a heavy mediator. Orange curves show the reach for the low-threshold scenario, and green curves show the reach for the high-threshold scenario. Projections for the standard halo, simple halo, and fast halo scenarios are shown by the solid, dotted, and dot-dashed curves, respectively. **Right:** projected reach for a 1 kg-yr exposure of a Dirac material, Si, and the two Al superconductor configurations assuming a heavy scalar or vector mediator. The parameters of the Dirac material are taken as in Fig. 2, with gap $2\Delta = 20\,\mathrm{meV}$, Fermi velocity $v_F = 4 \times 10^{-4}$, background dielectric constant $\kappa = 40$, and Dirac band cutoff $\omega_{\mathrm{max}} = 0.5\,\mathrm{eV}$. The projected reach for Si assumes a two-electron ionization threshold. The projected reach of URu_2Si_2 lies above the top edge of the plot. All curves assume the standard halo model. For the Al target, the shaded regions indicate the range of variation in different models of the loss function. The solid lines are computed using the GSRF loss function without damping, and the top of each shaded band is computed using the Lindhard loss function. An example of the target parameter space for thermal freeze-out through a heavy dark photon mediator [13] is shown in dashed blue.

(defined with respect to the ordinary electromagnetic fine-structure constant $\alpha_{\mathrm{EM}} \simeq 1/137$) and 'heavy mediator' means $m_\phi \gg \alpha_{\mathrm{EM}} m_e$. All reach projections are computed in the zero-temperature limit and assume that the detector is sensitive to deposits between 1 meV and 1 eV. We show reach curves for a high-threshold experiment sensitive to deposits 1 eV–1 keV for a heavy mediator in Fig. S6, along with recoil spectra for selected model points. We also illustrate the appearance of a feature in the recoil spectrum at ω_p in the fast halo model, where the plasmon peak is kinematically accessible. To facilitate comparison with the literature, we show reach curves corresponding to an event rate of $3\,\mathrm{kg}^{-1}\,\mathrm{yr}^{-1}$, which corresponds roughly to a 95% C.L. constraint.

Figure S5 in particular underscores the importance of properly treating the material response. For any interaction of the kind we consider in this work, screening is significant at low DM mass or for a light mediator. However, the implementation of screening in Ref. [6] overestimated the size of the effect for a vector mediator: at the lowest DM masses, the causal branch choice in the logarithms of Eq. (S.13) yields a rate as much as seven orders of magnitude greater than that produced by the acausal choice. Furthermore, accounting for the non-zero width of the plasmon peak further enhances the rate by an order of magnitude or more. The lingering uncertainty in analytical predictions of the loss function can be easily resolved by directly measuring the loss function in promising target materials.